Available online at www.sciencedirect.com
SCIENCE DIRECT®
Remote Sensing of Environment 89 (2004) 217–233
Remote Sensing of Environment
www.elsevier.com/locate/rse

Systematic corrections of AVHRR image composites for temporal studies

J. Cihlar[a,*], R. Latifovic[a], J. Chen[a,b], A. Trishchenko[a], Y. Du[c], G. Fedosejevs[a], B. Guindon[a]

[a] Canada Centre for Remote Sensing, 588 Booth Street, Ottawa, ON, Canada K1A 0Y7
[b] Department of Geography, University of Toronto, Canada
[c] Intermap Technologies Ltd., Canada

Received 16 February 2001; received in revised form 7 November 2001; accepted 15 June 2002

Abstract

For quantitative studies of vegetation dynamics, satellite data need to be corrected for spurious effects. In this study, we have applied several changes to an earlier advanced very high resolution radiometer (AVHRR) processing methodology (ABC3; [Remote Sens. Environ. 60 (1997) 35; J. Geophys. Res.-Atmos. 102 (1997) 29625; Can. J. Remote Sens. 23 (1997) 163]), to better represent the various physical processes causing contamination of the AVHRR measurements. These included published recent estimates of the NOAA-11 and NOAA-14 AVHRR calibration trajectories for channels 1 and 2; the best available estimates for the water vapour, aerosol and ozone amounts at the time of AVHRR data acquisition; an improved bidirectional reflectance algorithm that also takes into consideration surface topography; and an improved image screening algorithm for contaminated pixels. Unlike the previous study that compared the composite images to a single-date AVHRR image, we employed coincident TM images to approximate the AVHRR pixel field of view during the data acquisition. Compared to ABC3, the modified procedure ABC3V2 was found to improve the accuracy of AVHRR pixel reflectance estimates, both in the sensitivity (slope) of the regression and in r^2. The improvements were especially significant in AVHRR channel 1. In comparison with reference values derived from two full TM scenes, the corrected AVHRR surface reflectance estimates had average standard errors values of ± 0.009 for AVHRR C1, ± 0.019 for C2, and ± 0.04 for NDVI; the corresponding r^2 values were 0.55, 0.80, and 0.50, respectively. The changes in ABC3V2 were not able to completely remove interannual variability for land cover types with little or no vegetation cover, which would be expected to remain stable over time, and they increased the interannual variability of mixed forest and grassland. These results are attributed to a combination of increased sensitivity to interannual dynamics on one hand, and the inability to remove all sources of noise for barren or sparsely vegetated northern land cover types on the other.

Keywords: AVHRR; Pixel reflectance; Algorithm

1. Introduction and objectives

So far, data from the National Oceanic and Atmospheric Administration (NOAA) advanced very high resolution radiometer (AVHRR) have proven to be the longest and most comprehensive record of the seasonal and interannual behaviour of the earth's terrestrial biosphere (Townshend, 1994). Although higher quality data are becoming available from SPOT4/VEGETATION (Saint, 1992), MODIS (Barnes, Pagano, & Salomonson, 1998), MERIS, and GLI, AVHRR will remain vital component of the satellite data historical record and will, because of the need for the longest possible time series, continue to be important for earth system studies, including the understanding of long-term variability and change in land cover.

In practice, AVHRR data suffer from numerous limitations that make their use for biosphere studies problematic. They include marginally satisfactory calibration information, ground target signal contamination by atmospheric and surface effects, and changes in satellite orbit characteristics among and within missions. Thus, considerable effort has been spent by numerous research groups to process the data in a way that would make them suitable for quantitative land surface analysis. These efforts have been concerned with the

* Corresponding author.
E-mail address: josef.cihlar@ccrs.nrcan.gc.ca (J. Cihlar).

0034-4257/$ - see front matter © 2003 Published by Elsevier Inc.
doi:10.1016/j.rse.2002.06.007

volume production of basic image composites from which the effect of most clouds would be removed (Eidenshink & Faundeen, 1994; El Saleous et al., 2000; Holben, 1986; Robertson et al., 1992; Townshend, Huang, Kalluri, DeFries, & Liang, 2000) or with further processing to remove residual noise of various types from the composites (Cihlar, Ly, et al., 1997; Gutman, 1994; Los, Justice, & Tucker, 1994; Sellers et al., 1994). The primary sources of noise in the AVHRR composites are residual clouds, atmospheric contamination, bidirectional reflectance distribution factor (BRDF) effects, and particularly discrepancy in calibration between different platforms. To deal with these, Cihlar, Ly, et al. (1997) described a procedure dubbed ABC3 (Atmospheric, Bidirectional, and Contamination Corrections of CCRS) in which AVHRR 10-day composites were further processed to: update the radiometric calibration to that currently best known; identify contaminated pixels, both to be corrected and to be avoided in deriving BRDF coefficients, and substitute contaminated measurements by approximate values determined from the seasonal trajectory of the image variables.

AVHRR data covering the Canadian landmass were adjusted using ABC3 and used in various studies (Chen, Chen, Liu, Cihlar, & Gray, 2000; Chen, Chen, Price, Cihlar, & Liu, 2000; Cihlar, Beaubien, Latifovic, & Simard, 1999; Cihlar, Beaubien, Xiao, Chen, & Li, 1997; Cihlar et al., 1998; Cihlar, Chen, & Li, 1997; Fraser, Li, & Cihlar, 2000; Liu, Chen, Cihlar, & Chen, 1999; Liu, Chen, Cihlar, & Park, 1997). Through this experience, limitations in the correction procedures were identified and potential improvements were explored. Here, we describe an improved version of ABC3, dubbed ABC3V2. After discussing the rationale and principles of several enhancements, we evaluate their effectiveness using Landsat thematic mapper (TM) data as well as by examining the interannual consistency.

2. ABC3V2 procedure

Fig. 1 shows a flowchart of the modified procedure. Compared to the first version, the following main improvements were made:

- Atmospheric corrections for channels 1 (C1) and 2 (C2) to include the effects of local topography;
- Land cover type-dependent detection of contaminated pixels;
- Pixel- and date-specific estimates of water vapour and ozone content, and pixel-specific estimates of atmospheric pressure to be used in atmospheric corrections;
- Channel 3 (C3) processed to retrieve the solar reflected component and correct it for BRDF effects;
- Bidirectional correction to take into account the hot spot effect, NDVI (surface reflectance) and local topography;
- Aerosol optical depth based on more extensive measurements.

Input data for ABC3V2 are nine image composite layers: top-of-atmosphere (TOA) radiance for AVHRR channels 1–5, solar zenith angle θ_0, view zenith θ, relative azimuth $\Delta\phi$, and date of imaging for each pixel. The compositing step, i.e., selection of the clearest pixel among those observed over a time period, is based on the maximum value of the normalised difference vegetation difference (NDVI). If warranted, C1 and C2 data are recalibrated by first retrieving the raw signal values and then introducing the more correct calibration coefficients, while retaining full radiometric resolution of the original data along the way. The calibration of thermal channels 3–5 follows the NOAA recommended procedure (Kidwell, 1998) and uses scene-averaged calibration coefficients derived from in-flight measurements of calibration sources. After computing atmospheric corrections, the likelihood of residual atmospheric or surface (e.g., snow) contamination in individual pixels is determined. Bidirectional reflectance corrections are made for channels 1, 2, and 3, by using information on the imaging geometry, land cover, and the terrain slope. Atmospheric and surface emissivity corrections are then derived for channels 4 and 5; no changes were made in this aspect relative to ABC3. The solar reflected part of C3 is isolated from the initial measurement and corrected for BRDF effects. Finally, contaminated pixels are replaced in all channels by using (i) the values measured for the period, (ii) those from other periods, and (iii) assumptions regarding temporal continuity. The new steps or modifications in relation to the original version (Cihlar, Ly, et al., 1997) are described below.

2.1. Atmospheric corrections incorporating local topographic effects

Through the scattering and reflection of solar radiation in the surface-atmosphere system, the atmospheric correction of satellite measurement is linked to local topography of a pixel and its surrounding area (Proy, Tanre, & Deschamps, 1989; Richter, 1998; Sandmeier & Itten, 1997; Teillet, Guindon, & Goodenough, 1982; Vermote, Tanre, Deuze, Herman, & Mocrette, 1997). Two surface features play a major role in determining apparent radiance at the TOA, surface inclination, and the structure of rugged relief surrounding the pixel. Surface inclination changes the geometry of reflection, while the second factor changes the amount of diffuse radiation reaching the pixel region, thus producing reflection from neighbouring areas and also creating shadows by blocking the direct solar beam. The correction approach is described first with respect to the effect of an inclined surface on the amount of radiation reaching the surface, and the corrections at the TOA level are given subsequently.

2.1.1. Surface level

We denote the surface slope of a pixel as β and the surface aspect angle as γ (measured clockwise relative to

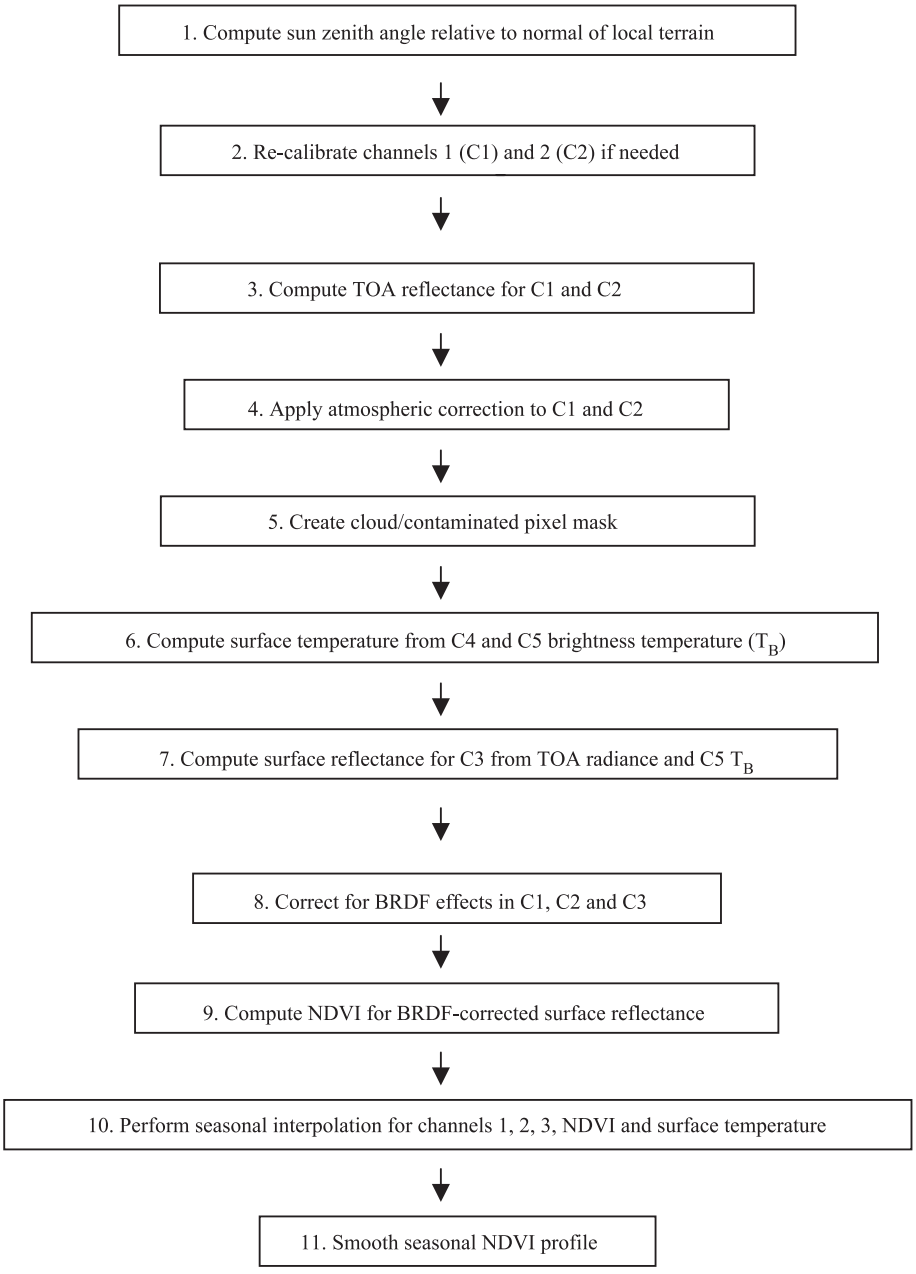

Fig. 1. Flowchart for the ABC3V2 data processing.

North) and use superscript * to refer to parameters of an inclined surface (Fig. 2).

Solar and satellite zenith angles θ_0^* and θ^* relative to the normal of an inclined surface are (Iqball, 1983):

$$\cos\theta_0^* = \cos\beta\cos\theta_0 + \sin\beta\sin\theta_0\cos(\gamma - \phi_s) \quad (1a)$$

and

$$\cos\theta^* = \cos\beta\cos\theta + \sin\beta\sin\theta\cos(\gamma - \phi), \quad (1b)$$

where ϕ_s is the solar azimuth and ϕ is the satellite azimuth. Since only solar zenith angle θ_0, satellite zenith angle θ, and relative azimuth angle $\Delta\phi = \phi_s - \phi$ were provided in the GEOCOMP composite images (Robertson et al., 1992) used as input to ABC3V2, a special procedure was applied to compute sun and satellite azimuth angles employed in Eqs. (1a) and (1b). First, the imaging time was computed by iteratively solving the algorithm for sun zenith angle to find the time at which the sun zenith angle matches the angle recorded in the composite image. The imaging time was then used to compute the sun azimuth angle. Expressions employed to compute the sun-earth distance, solar declination, and the equation of time were taken from Iqball (1983) and Spencer (1971).

The downward global irradiance, G, at the surface consists of two parts, direct (B) and diffuse (D) irradiance:

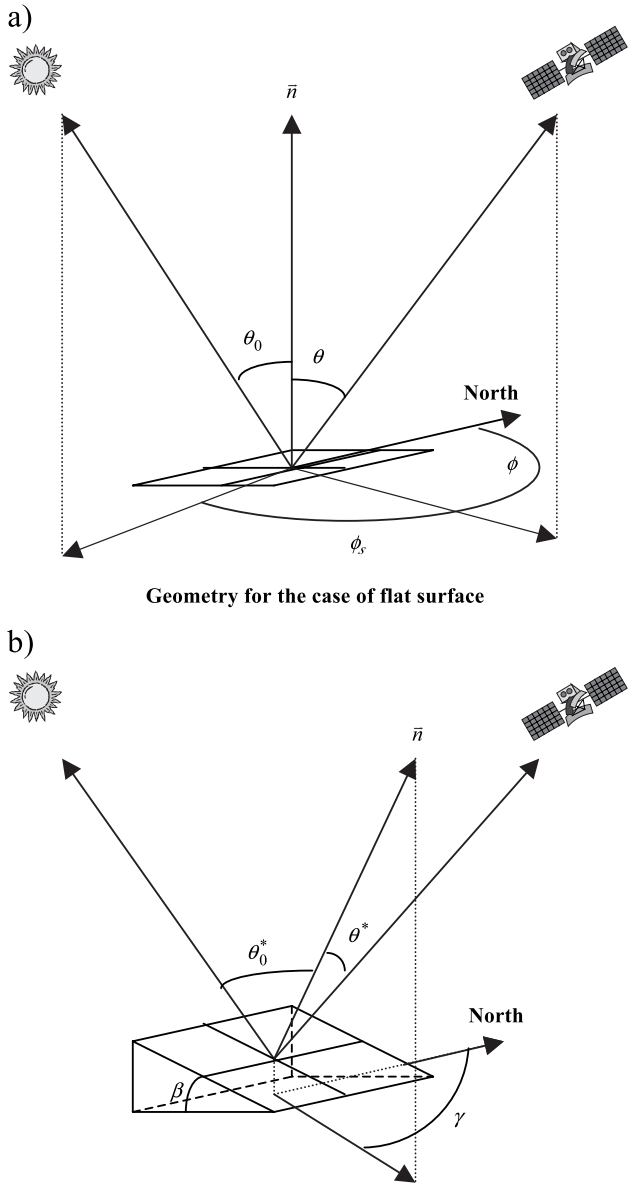

Fig. 2. Geometric configuration of the corrections for an inclined surface.

$G = B + D$. B is the solar irradiance coming from the direction of the Sun and attenuated by the atmosphere, while D results from molecular and aerosol scattering as well from multiple reflections and scattering between the surface and the atmosphere. The correction due to surface inclination for the direct component is straightforward:

$$B^* = B_0 \cos\theta_0^* \Theta(90^0 - \theta_0^*) = \frac{B}{\cos\theta_0} \cos\theta_0^* \Theta(90^0 - \theta_0^*) = B r_b \Theta(\cos\theta_0^*), \quad (2)$$

where $r_b = \cos\theta_0^*/\cos\theta_0$, B_0 is direct solar irradiance for normal incidence, B is direct solar irradiance for the horizontal surface, B^* is direct solar irradiance for an inclined surface, and

$$\Theta(x) = \Theta(90^0 - \theta_0^*) = \Theta(\cos\theta_0^*)$$

is a step function, which is equal to 1 for an argument ≥ 0 and 0 otherwise. It is used here to set the direct solar irradiance to zero for a shadowed pixel.

The transformation for diffuse irradiance is more complicated. Rugged terrain can obscure part of the sky hemisphere and/or reflect some radiation from neighbouring pixels, thereby modifying the diffuse irradiance that reaches the pixel under consideration. Furthermore, the angular distribution of diffuse irradiance is non-isotropic. Because an exact analytical solution is not available for the general case, we adopted a simple model proposed by Hay (1985), which takes into account both above factors. It is modified here to include reflection from the surrounding area in the manner similar to Richter (1998):

$$D^* = D\{\Theta(\mu_0^*) t_s(\theta_0) r_b + [1 - \Theta(\mu_0^*) t_s(\theta_0)] V_{sky}\} + \rho_e \frac{G}{\pi}(1 - V_{sky}), \quad (3)$$

where $\mu_0^* = \cos\theta_0^*$, $t_s(\theta_0)$ is atmospheric transmission for the direct solar irradiance, ρ_e is the reflectance of the surrounding area, and V_{sky} is the so-called configuration or sky-view factor, proportional to the solid angle corresponding to the non-obscured portion of the sky hemisphere. Atmospheric direct transmission $t_s(\theta_0)$ and diffuse transmission $t_d(\theta_0)$are defined as:

$$t_s(\theta_0) = \frac{B(\theta_0)}{S_0 \mu_0} \text{ and } t_d(\theta_0) = \frac{D(\theta_0)}{S_0 \mu_0}, \quad (4)$$

where S_0 is the solar constant for a specific spectral channel. The sky-view factor is defined as

$$V_{sky} = \frac{1}{\pi} \int_0^{2\pi} da \int_0^{\pi/2 - h(\Phi)} d\Phi \cos(\Phi) \sin\Phi,$$

where Φ is zenith angle of the sky point relative to the normal of the pixel, a is azimuth of the sky point, and h is the elevation for azimuth a.

The first term in Eq. (3) represents the contribution of circumsolar (forward peak) radiation and the second term describes the contribution of isotropic radiation. We used weight $t_s(\theta_0)$ (Eq. (4)) to establish a balance between these two components in the diffuse field. The computation of $t_s(\theta_0)$ and $t_d(\theta_0)$ needed in Eqs. (3) and (4) is explained later. The third term in Eq. (3) represents the contribution of radiation reflected from the area surrounding the pixel. Due to the limited knowledge of elevation h and for the sake of

computational efficiency, we use simple parameterisation for V_{sky} proposed by Kondratyev (1977):

$$V_{sky} = \frac{1}{2}(1 + \cos\beta). \quad (5)$$

Therefore, for the total radiation on the inclined surface G^*, we derived the following approximation:

$$G^* = B^* + D^* = Br_b\Theta(\mu_0^*) + D\{\Theta(\mu_0^*)t_s(\theta_0)r_b + [1 - \Theta(\mu_0^*)t_s(\theta_0)]V_{sky}\} + \rho_e\frac{G}{\pi}(1 - V_{sky}). \quad (6)$$

2.1.2. TOA level

The Simplified Method for Atmospheric Corrections (SMAC algorithm; Rahman & Dedieu, 1994) was employed in ABC3 for atmospheric correction of the satellite measurements. SMAC accounts for gaseous transmission as well as for aerosol scattering and absorption. It also accounts for the Rayleigh scattering, which is a strong function of wavelength and is more important for shorter wavelengths, low sun elevations, and larger view angles. The method requires vertically integrated amounts of different gaseous components, sun zenith angle θ_0, view zenith angle θ, relative azimuth angle $\Delta\phi$, and the value of aerosol optical depth at 550 nm for each pixel. Tests conducted by Rahman and Dedieu (1994) showed that the errors introduced by the parameterisation are small, but the accuracy decreases if the view and solar zenith angles are above 60° and 50°, respectively, or if the optical depth is above 0.8. The changes to the SMAC algorithm to account for topographic effects are explained below.

The basic equation used in SMAC to retrieve surface Lambertian reflectance from TOA apparent reflectance in case of a "flat" pixel is (Rahman & Dedieu, 1994):

$$\rho_T(\theta_0, \theta, \Delta\phi) = \rho_a(\theta_0, \theta, \Delta\phi) + \frac{[t_s(\theta_0) + t_d(\theta_0)][\rho_p t_s(\theta) + \rho_e t_d(\theta)]}{1 - \rho_e S} \quad (7)$$

where $\rho_T = \pi L_T/S_0\mu_0$ is TOA spectral reflectance measured by the satellite sensor, L_T is satellite measured radiance, ρ_a is atmospheric reflectance, $t_s(\theta)$ is direct, and $t_d(\theta)$ is diffuse transmittance defined in Eq. (4), ρ_p is the surface pixel reflectance, ρ_e is the average reflectance of the pixel and its surrounding area (reflecting into the sensor's field of view, assumed to be equal in the computation), and S is spherical albedo of the atmosphere. The detailed explanation and expressions for the dependence of ρ_a, $t_s(\theta)$, $t_d(\theta)$, and S upon gas abundances, aerosol optical properties, and atmospheric parameters can be found in Rahman and Dedieu (1994).

Using the definition of direct and diffuse transmittances from Eq. (4), Eq. (7) can be rewritten as:

$$\rho_T(\theta_0, \theta, \Delta\phi) = \rho_a(\theta_0, \theta, \Delta\phi) + \frac{\left[\frac{B(\theta_0) + D(\theta_0)}{S_0\mu_0}\right][\rho_p t_s(\theta) + \rho_e t_d(\theta)]}{1 - \rho_e S}. \quad (8)$$

To account for surface topography effects described above, the direct component $B(\theta_0)$ should be transformed to $B^*(\theta_0)$ and the diffuse $D(\theta_0)$to $D^*(\theta_0)$. With these changes implemented, the Eq. (8) becomes:

$$\rho_T(\theta_0, \theta, \Delta\phi) = \rho_a(\theta_0, \theta, \Delta\phi) + \frac{[t_s(\theta_0)r_b\Theta(\mu_0^*) + t_d(\theta_0)\{\Theta(\mu_0^*)t_s(\theta_0)r_b + [1 - \Theta(\mu_0^*)t_s(\theta_0)]V_{sky}\}][\rho_p t_s(\theta) + \rho_e t_d(\theta)]}{1 - \rho_e S} + \frac{\left[\frac{t_s(\theta_0) + t_d(\theta_0)}{\pi}\rho_e(1 - V_{sky})\right][\rho_p t_s(\theta) + \rho_e t_d(\theta)}{1 - \rho_e S}. \quad (9)$$

Eq. (9) can then be inverted to obtain the solution for surface reflectance. With an assumption of negligible reflection from the surrounding area, which is described by the third term in Eq. (9) and homogeneous surface reflectance, i.e., $\rho_p = \rho_e = \rho$, the solution is given by

$$\rho = \frac{\Delta\rho}{g^*T(\theta) + \Delta\rho S}, \quad (10)$$

where

$$\Delta\rho = \rho_T(\theta_0, \theta, \Delta\phi) - \rho_a(\theta_0, \theta, \Delta\phi),$$

$$g^* = t_s(\theta_0)r_b\Theta(\mu_0^*) + t_d(\theta_0)\{\Theta(\mu_0^*)t_s(\theta_0)r_b + [1 - \Theta(\mu_0^*)t_s(\theta_0)]V_{sky}\},$$

and

$$T(\theta) = t_s(\theta) + t_d(\theta).$$

The general solution of Eq. (9) for the surface reflectance in the case of homogeneous area is given by

$$\rho = \frac{\sqrt{(g^*T(\theta) + \Delta\rho S)^2 + 4\tilde{g}T(\theta)\Delta\rho} - g^*T(\theta) - \Delta\rho S}{2\tilde{g}T(\theta)}, \tag{11}$$

where

$$\tilde{g} = \frac{(1 - V_{sky})}{\pi}[t_s(\theta_0) + t_d(\theta_0)].$$

To compute the atmospheric transmittance t_s and t_d, SMAC requires values of integrated column water vapour (IWV) and ozone content, atmospheric pressure, and aerosol optical depth at 550 nm. Previously, constant values were used for these parameters (Cihlar, Ly, et al., 1997). In a more recent study of the sensitivity of atmospheric corrections to water vapour effects we have found (Cihlar, Tcherednichenko, Latifovic, Li, & Chen, 2001) that for Canada, NDVI differences up to 7.5% in relative terms during the peak green period could ensue if a constant value is assumed. We have also determined that due to the large IWV variability, pixel- and date-specific estimates should be used. Presently, the atmospheric reanalysis projects provide the only spatially and temporally consistent data set for Canada and many other areas of the world. For example, the NCAR reanalysis project (Kalnay et al., 1996) produced IWV estimates for 6-h periods on a 2.5° by 2.5° grid. Given a known date of acquiring each AVHRR pixel, an improved IWV estimate can be obtained through spatial interpolation. We used the 1800 GMT estimate and interpolated using inverse-square-distance weighting function (without a correction for altitude).

Similar to IWV, ozone concentration also affects radiance in C1 and C2, albeit to a lesser extent. Unlike the water vapour, ozone affects C1 more due to its being located in the ozone absorption band (*Chappius* band) centred on 600 nm. A varying ozone content within ± 50 Dobson Units (DU) around a reference value 350 DU for $\theta_0 < 45°$ and $\theta < 45°$ would change C1 reflectance by less than ± 0.004 for surface reflectances below 0.3. This corresponds to a relative uncertainty typically within ± 2%. The error increases for larger angles and may reach ± 0.009 in surface reflectance or ± 5–7% in relative uncertainty for a solar zenith angle of 75°. There is minimal ozone absorption in C2, causing changes of less than ± 0.0006 in surface reflectance or ± 0.1% in relative uncertainty for C2. The ozone impact on NDVI can be estimated from the simple expression,

$$\mathrm{NDVI}(\varepsilon) = \frac{R_2 - R_1(1 \pm \varepsilon)}{R_2 + R_1(1 \pm \varepsilon)},$$

where $R_{1,2}$ is C1(C2) reflectance and is relative change of C1 reflectance, which is assumed to be small; the change in C2 reflectance due to ozone variation is neglected. The reference value for the vegetation index is $\mathrm{NDVI}_0 = (R_2 - R_1)/(R_2 + R_1)$, which leads to the following relationship between channel reflectances

$$R_2 = R_1 \frac{1 + \mathrm{NDVI}_0}{1 - \mathrm{NDVI}_0}.$$

Thus, modified and reference values of NDVI are related to each other as

$$\begin{aligned}
\mathrm{NDVI}(\varepsilon) &= \frac{(1 + \mathrm{NDVI}_0)/(1 + \mathrm{NDVI}_0) - (1 + \varepsilon)}{(1 + \mathrm{NDVI}_0)/(1 + \mathrm{NDVI}_0) + (1 + \varepsilon)} \\
&= \frac{(1 + \mathrm{NDVI}_0) - (1 + \varepsilon)(1 - \mathrm{NDVI}_0)}{(1 + \mathrm{NDVI}_0) + (1 + \varepsilon)(1 - \mathrm{NDVI}_0)} \\
&= \frac{2\mathrm{NDVI}_0 - \varepsilon(1 - \mathrm{NDVI}_0)}{2 + \varepsilon(1 - \mathrm{NDVI}_0)} \\
&= \frac{\mathrm{NDVI}_0 - \frac{\varepsilon}{2}(1 - \mathrm{NDVI}_0)}{1 + \frac{\varepsilon}{2}(1 - \mathrm{NDVI}_0)} \\
&\approx \mathrm{NDVI}_0 - \frac{\varepsilon}{2}(1 - \mathrm{NDVI}_0^2)
\end{aligned} \tag{12}$$

As seen from Eq. (12), ozone impact on NDVI has the opposite sign to C1 reflectance. The relative effect is greater than in C1 for NDVI < 0.4 and smaller than in C1 for larger values. The absolute magnitude of the change is typically less than 0.015.

Spatial data sets of atmospheric ozone content derived from satellite measurements are also available. We have used the daily (total column) ozone data obtained by TOMS on Meteor 3 (Herman et al., 1996). Given that the main ozone variability is seasonal, we aggregated the daily data (August 1991 to November 1994) into a single annual set of monthly averages. These gridded data with a resolution of 1° latitude by 1.25° longitude were spatially interpolated to 1-km pixels using an inverse-square-distance weighting function (without a correction for altitude). The monthly average values were then used for each pixel in a composite according to the month.

A constant value of atmospheric pressure was previously used in ABC3. The main source of variability is due to the local depth of the atmospheric column, with possible additional seasonal effects. To account for both effects, the atmospheric pressure data from the NCAR reanalysis (Kalnay et al., 1996) for 12-h periods and the mean terrain elevation on a 1.875° latitude by 1.875° longitude grid were averaged for the growing season (April to September) over a 5-year period (1993–1997). Based on the relationship between elevation and pressure P ($P = 1014.2e^{-0.0001*h}$, h = geopotential height in millibars, $r^2 = 0.998$), the pressure was estimated for each pixel using an existing digital elevation model resampled to 1-km pixels.

For aerosol optical depth, a constant value has again been used in ABC3V2. This is necessitated by the lack of

better data and justified by sunphotometer measurements acquired at several sites across Canada over several years by the AEROCAN aerosol network. The value of 0.06 at 550 nm gives a good single-value representation of the aerosol optical depth (Fedosejevs et al., 2000), in spite of some variability due to smoke from biomass burning and other effects. This value is close to 0.05 as used in ABC3. When wildfires are active, the aerosol amount changes daily. The effect of aerosol on the surface reflectance calculation can thus be further improved when spatially explicit daily aerosol data become available.

2.2. Pixel contamination

When one is interested in the biospheric signal from the land surface, AVHRR data may be contaminated by thin or subpixel clouds, heavy aerosol, or by snow covering the pixel or its part. In ABC3, the CECANT algorithm (Cihlar, 1996) was used, based on the Fourier transform approximation of NDVI (surface reflectance) trajectory (Los et al., 1994; Sellers et al., 1994). CECANT uses the seasonal NDVI (surface reflectance) trajectory for each pixel and C1 surface reflectance. Since all the above contamination sources decrease the pixel's contrast between C1 and C2 (Holben, 1986), NDVI is rather sensitive to small atmospheric effects, including fog, subpixel snow, etc.

Experience with the data processed using ABC3 showed that the Fourier transform approximation is not optimal for all land cover types. In particular, NDVI for coniferous forests is rather flat during the growing season. After investigating various possibilities, Cihlar, Du, and Latifovic (in press) developed an algorithm, which combines the Fourier transform and a second order polynomial. They also simplified CECANT further so that the effect of NDVI is captured by one parameter (R_r below). The modified CECANT thus requires only three thresholds: a coarse C1 surface reflectance threshold to screen out snow-covered pixels (a constant value of 0.3 is used) and two date- and land cover type-dependent thresholds for R_r. These parameters are derived dynamically from the growing season data set itself. R_r is computed as follows:

$$R_r(i,j,t) = (R(i,j,t) - R_m(t)) \times \cos(\arctan(b(t))) + (Z(i,j,t) - Z_m(t)) \times \sin(\arctan(b(t))), \quad (13)$$

$$R(i,j,t) = \frac{\mathrm{NDVI}(i,j,t) - \mathrm{NDVI}_a(i,j,t)}{M(i,j)},$$

$$Z(i,j,t) = \frac{\mathrm{NDVI}_{max}(i,j,t) - \mathrm{NDVI}(i,j,t)}{\mathrm{NDVI}_{max}(i,j,t)},$$

where: NDVI_{max} and NDVI_a are the expected uncontaminated NDVI values, $R_m(Z_m)$ is the mean $R(Z)$ value for a compositing period t, $i(j)$ is the line (pixel) number, M is the median for the absolute difference $|\mathrm{NDVI} - \mathrm{NDVI}_a|$, and b is the slope of the principal axis in the $R - Z$ space. NDVI_a and NDVI_{max} are estimated using a Fourier transform applied to the measured NDVI (surface reflectance) values (Cihlar, 1996; Cihlar, Du, et al., in press).

Eq. (13) is applied separately to pixels for each land cover type, a cover type map is therefore a required input.

2.3. Bidirectional reflectance corrections

Cihlar, Ly, et al. (1997) described a procedure for BRDF corrections in which the pixel surface reflectance is normalised to nadir at a constant solar zenith angle of 45°. These corrections used the model of Wu, Li, and Cihlar (1995), based on the work of Roujean, Leroy, and Deschamps (1992). The model coefficients were derived using uncontaminated pixels during the entire season as determined by CECANT, separately for major land cover types. However, because of the changing orbital characteristics of AVHRR and the somewhat zonal distribution of land cover, the sample of contaminated pixels was not necessarily optimal in terms of the observation geometry. Cihlar et al. (1998) concluded that a better strategy would be to establish land cover type-dependent (but not year-dependent) BRDF model coefficients from several years of data; this would also avoid the necessity of first determining the clear pixels.

A second deficiency of the original procedure is related to surface slope. While the assumption of a flat surface in ABC3 is reasonable at AVHRR resolutions for a substantial part of Canada, it is completely inadequate for the mountainous regions of Canada. Since quality digital elevation models have become available recently (CFS, 1998), we were able to incorporate these in the BRDF corrections.

Thirdly, after analysing the data processed by ABC3, we have found that significant hot spot effects may remain in some AVHRR data that were not accounted for by the models of Roujean et al. (1992) or Wu et al. (1995). Since then, a correction suitable for AVHRR data was developed by Chen and Cihlar (1997), based on a simplification of the four-scale model of Chen and Leblanc (1997). To avoid the need for date-dependent coefficients, NDVI was used as an independent variable (see also Latifovic, Cihlar, & Chen, 2003; Wu et al., 1995).

Taking all these effects into account, the BRDF corrections for C1 and C2 thus have the form:

$$\rho(\theta_0,\theta,\phi) = \begin{bmatrix} 1 + (a_1 + a_2{*}\mathrm{NDVI} + a_3{*}\mathrm{NDVI}^2){*}f_1(\theta_0,\theta,\phi) + \\ (a_4 + a_5{*}\mathrm{NDVI} + a_6{*}\mathrm{NDVI}^2){*}f_2(\theta_0,\theta,\phi) \end{bmatrix} * \left[1 + a_7 e^{-\frac{\xi}{\pi}a_8}\right]; \quad (14)$$

$$\cos\xi = \cos\theta_0^*\cos\theta^* + \sin\theta_0^*\sin\theta^*\cos\phi;$$

$$f_1(\theta_0,\theta,\phi) = \frac{1}{2\pi}[(\pi-\phi)\cos\phi + \sin\phi]\tan\theta_0^*\tan\theta^* - \frac{1}{\pi}(\tan\theta_0^* + \tan\theta^* + \sqrt{\tan^2\theta_0^* + \tan^2\theta^* - 2\tan\theta_0^*\tan\theta^*\cos\phi});$$

$$f_2(\theta_0,\theta,\phi) = \frac{4}{3\pi} * \frac{1}{\cos\theta_0^* + \cos\theta^*} \times \left[\left(\frac{\pi}{2} - \xi\right)\cos\xi + \sin\xi\right] - \frac{1}{3};$$

where $\rho_{s,i}$ denotes the reflectance in AVHRR channel i, $f_1$describes the bidirectional dependence due to diffuse reflection from opaque reflectors on the ground and to the shadowing effects of the leaves, and f_2 accounts for the contribution of the volume scattering by a collection of randomly dispersed facets of canopy and bare soil. Both f_1 and f_2 depend on the solar, view, and azimuth angles.

2.4. Estimation of surface reflectance in AVHRR channel 3

The radiance as measured by AVHRR channel 3 (C3) contains thermal emissive and reflective components. Thermal emission arises from atmospheric and surface thermal sources. The reflective component contains solar and thermal flux reflected by the surface and the atmosphere. The solar reflected component of C3 is of interest because of its spectral uniqueness, but it needs to be isolated from the total signal in this spectral channel.

The general expression for satellite measured radiance at the TOA level for a cloud-free atmosphere in C3 can be written as a simple energy balance equation:

$$L_3 = t_3(\theta_0,\theta)\rho_3\frac{S_{0.3}}{\pi}\mu_0 + \tau_3(\theta) \times \left[\varepsilon_3 B(\lambda_3, T_s) + \rho_3 L_{atm,3}\downarrow\right] + L_{atm,3}\uparrow, \quad (15)$$

where $t_3(\theta_0,\theta)$ is two-way total atmospheric transmittance (sun-surface-sensor), ρ_3 is surface reflectance in C3, $S_{0,3}$ is the nominal solar constant in C3, $\tau_3(\theta)$ is one-way total atmospheric transmittance (from surface to sensor), so that $t_3(\theta_0,\theta) = \tau_3(\theta_0,\theta)$, ε_3 is surface emissivity in C3, $B(\lambda_3,T_s)$ is black-body radiation corresponding to surface temperature T_s, and C3 central wavelength ($\lambda_3 = 3.779$ μm for AVHRR onboard NOAA-14).

The expression (15) assumes that ρ_3 and ε_3 are angle-independent (Lambertian surface). Because the surface is opaque in this spectral region, we can relate these parameters to each other as

$$\rho_3 = 1 - \varepsilon_3.$$

The solution of Eq. (15) for surface reflectance ρ_3 employing the above relation is

$$\rho_3 = \frac{L_3 - \tau_3(\theta)B(\lambda_3,T_s) - L_{atm,3}\uparrow}{t_3(\theta_0,\theta)\frac{S_{0,3}}{\pi}\mu_0 - \tau_3(\theta)B(\lambda_3,T_s) + \tau_3(\theta)L_{atm,3}\downarrow} \quad (16)$$

As discussed elsewhere (Gessell, 1989; Ruff & Gruber, 1983), there is an essential mutual compensation of attenuation and thermal emission terms, so that one can approximately assume the transmittances (t_3 and τ_3) to be equal to 1.0 and neglect atmospheric downward and upward thermal emission terms. With this approximation, Eq. (16) becomes:

$$\rho_3 = \frac{L_3 - B(\lambda_3,T_s)}{\frac{S_{0,3}}{\pi}\mu_0 - B(\lambda_3,T_s)}. \quad (17)$$

Kaufman and Remer (1994) estimated the accuracy of Eq. (17) to be around ± 0.01 to ± 0.02 and slightly worse for surface temperatures above 300 K. Eq. (17) has also been used in a number of other studies (e.g., Barbosa, Gregoire, & Pereira, 1999; Holben & Shimabukuro, 1993; Pereira, 1999; Roy, Giglio, Kendal, & Justice, 1999). Here, we also employed this expression for retrieving surface reflectance in C3, using AVHRR channel 5 uncorrected brightness temperature as an approximation of T_s. To account for a possible C3 saturation above 320 K as well for neglecting atmospheric effects and surface emissivity effect in channel 5, we introduced an offset of $+0.05$. Although Eq. (17) for computing ρ_3 is convenient for operational use, it is to some extent an oversimplified model, which may be less accurate at low sun elevations and some other extreme conditions (Roger & Vermote, 1998). A more sophisticated model is under development and will be employed in the future for the retrievals of C3 surface reflectance.

3. Data

AVHRR data covering the landmass of Canada from two satellite platforms, NOAA-11 (1993–1994) and NOAA-14 (1995–1998) were used. The initial composites were created by processing daily images of Canada's landmass using the GEOCOMP system (Robertson et al., 1992). Briefly, GEOCOMP performs sensor calibration using the best known estimate of the calibration coefficients at the time of processing; subpixel-accuracy geocoding of all images using an orbital model and high resolution image chips; transformation to a Lambert Conformal Conic projection; resampling of the images to a 1-km pixel size; and compositing for 10-day periods using the maximum NDVI criterion. Further details on GEOCOMP processing are provided by Cihlar, Chen, et al. (1997). The ABC3V2 corrections described in the previous section were applied to all 10-day composites between 11 April and 31 October for 1993–1998.

To evaluate the radiometric quality of the resulting surface reflectances, C1 and C2 values were compared with reflectances in two Landsat TM scenes (bands 3 and 4, respectively). The TM surface reflectance values corresponding to the AVHRR 1-km pixels in the composites were obtained as follows. Two summer Landsat 5 scenes with a variety of land cover types were selected of Quebec (path 20, row 25, 5 August 1998) and Alberta (path 48, row 22, 29 August 1998), respectively. The scenes at 30 m resolution were first registered using ground control points obtained from 1:50,000 topographic maps. The procedure for geolocation at AVHRR sub-pixel level of resampled TM was developed based on digital image matching (Guindon,1985). These data were then corrected for atmospheric effects using 6S (Vermote et al., 1997) with inputs of scene-specific atmospheric conditions. The same atmospheric water column data (Kalnay et al., 1996) and ozone thickness (McPeters et al., 1998), taken as the average over an entire scene, were used as one of the inputs. The aerosol optical depth estimates were obtained from using the algorithm by Fallah-Adl, Jaja, and Liang (1997) based on a dark object method. Further details on the atmospheric corrections are provided by Chen, Pavlic, et al. (2000). Using these corrected data, the equivalent AVHRR values for each 1-km pixel were then determined by assuming that the modulation transfer function (MTF) of AVHRR has a Gaussian shape with a standard deviation (1σ) of ± 800 m; the chosen standard deviation corresponds to the uncertainty of GEOCOMP processing, which has been found to be ± 600 m or less (Cihlar et al., 1998).

The MTF was applied to a constant window $\pm 3\sigma$ in both directions. In other words, an attempt was made to re-

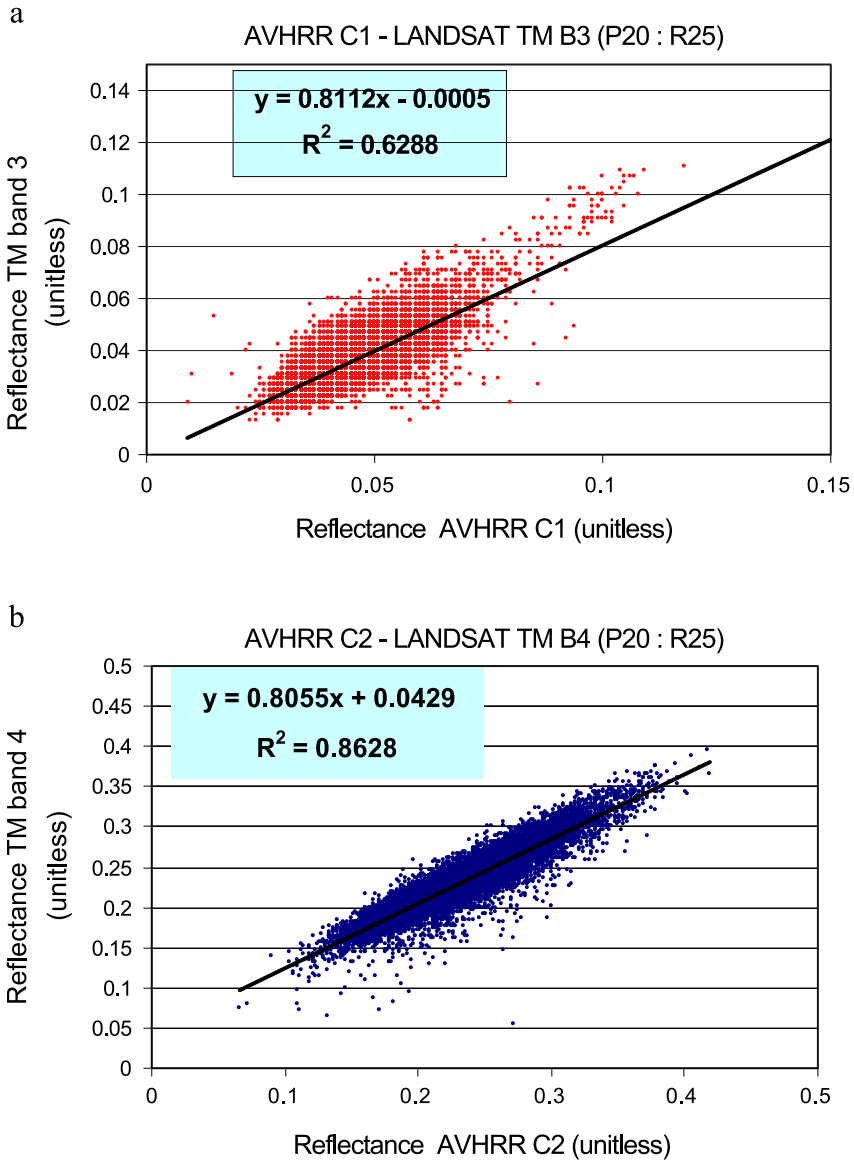

Fig. 3. Comparison of corrected AVHRR data with time-coincident Landsat TM data. (a) Surface red reflectance, (b) surface near infrared reflectance, (c) surface NDVI, (d) top-of-the-atmosphere red reflectance.

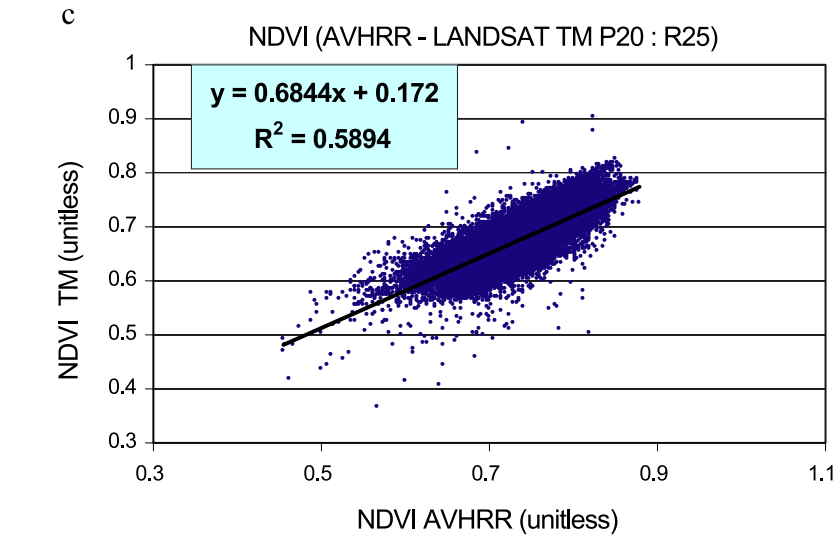

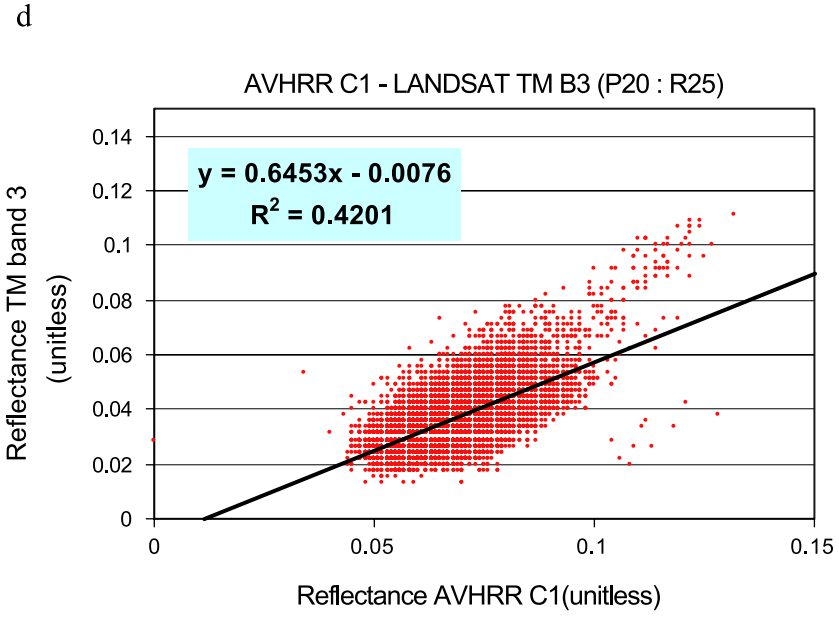

Fig. 3 (*continued*).

create the original AVHRR measurement. The TM pixel corresponding to the centre of the MTF window was located through coincident geographic coordinates. No corrections were made to account for differences in the spectral bandwidths. To avoid pixels containing open water, open water bodies (water class in the map of Cihlar et al., 1999) were masked out including a four-pixel buffer zone around these. Similarly, visible clouds were masked out from the TM images before the comparison.

As a second comparison, the interannual trends observed in the corrected data were evaluated. The results of this evaluation were compared with results of a study of the sensitivity of AVHRR for detecting interannual changes (Cihlar et al., 1998). To facilitate this comparison, the same corresponding sites were employed as in the previous study.

4. Results and discussion

4.1. Comparison with Landsat TM data

Fig. 3 compares surface reflectance values obtained for one TM scene in Quebec for the corresponding 1 km^2 areas and the same period (1998/08/05 for TM scene, 1998/08/01–10 for AVHRR composite). For AVHRR C1, the corrected values are distributed along the 1:1 line, but the best fit line deviates from this trend with a slope of 0.8. The r^2 is also relatively high (0.63), given the narrow range of the values (~ 0.03–0.07). It appears, however, that a further improvement could be obtained if the AVHRR values were reduced more. This is partly indicated by a comparison of TOA AVHRR values against surface TM (Fig. 3d). The extension to higher AVHRR values is evident

Table 1
Comparison of the correctedAVHRR data with reference data sets

TM scene	Channel	Statistics						Mean reflectance			CV***	
		Surface			TOA			Surface TM	Surface AVHRR	TOA AVHRR	Surface AVHRR	TOA AVHRR
		Slope	r^2**	S.E. Y	Slope	r^2**	S.E. Y					
20–25*	C1	0.81	0.63	0.006	0.65	0.42	0.007	0.035	0.044	0.066	13%	11%
	C2	1.07	0.86	0.015	0.95	0.72	0.018	0.224	0.224	0.210	7%	9%
	NDVI	0.86	0.59	0.034	0.74	0.44	0.039	0.729	0.671	0.517	5%	8%
44–22**	C1	0.58	0.46	0.011	0.13	0.04	0.015	0.038	0.056	0.072	20%	21%
	C2	0.77	0.73	0.023	0.47	0.29	0.038	0.216	0.240	0.217	10%	17%
	NDVI	0.73	0.41	0.054	0.42	0.18	0.064	0.705	0.626	0.504	9%	13%
20–25 and 44–22	C1	0.573	0.472	0.009	0.207	0.081	0.012	0.037	0.050		17%	16%
	C2	0.746	0.717	0.02	0.565	0.367	0.032	0.220	0.232		8%	13%
	NDVI	0.735	0.479	0.046	0.514	0.252	0.055	0.717	0.648		7%	10%
AVHRR (Cihlar, Beaubien, et al., 1997c; Cihlar, Chen et al., 1997b; Cihlar, Ly et al., 1997a)	C1	0.260	0.060	0.014					0.050		28%	
	C2	0.740	0.450	0.040					0.230		17%	
	NDVI	0.600	0.330	0.066					0.640		10%	
Improvement (ABC3V2 vs. ABC3V1)	C1	128%	686%	−35%							68%	
	C2	0.81%	59%	50%							113%	
	NDVI	22%	45%	−30%							51%	

The regression relation for statistics: TM = $a + b$*AVHRR.

* Acquired August 5, 1998; number of pixels for comparisons $N = 23599$.

** Acquired August 29, 1998; number of pixels for comparisons $N = 27{,}756$.

*** Coefficient of variability.

and is due to measurements obtained at high θ_s angles. These higher values were insufficiently accounted for by the atmospheric and BRDF corrections. A similar phenomenon was observed in the other TM scene (not shown).

Results for AVHRR C2 are even more consistent, with $r^2 = 0.86$. The slope of the line is also < 1.0, similarly as for C1. For NDVI (Fig. 3c), both the slope (0.68) and r^2 (0.59) are lower than for individual bands, possibly because of the narrower NDVI range (mostly 0.6–0.85, Fig. 3c).

Table 1 provides a comparison of the statistical relationships between the AVHRR and the corresponding TM-derived reflectance values for the two TM scenes.

Although the results varied somewhat between scenes, possibly due to differences in land cover and the quality of corrections, the combined statistics for the two scenes indicate several consistent trends:

- The regression slope and r^2 were significantly and consistently better for AVHRR C2 compared to C1 and NDVI, most likely reflecting the wider radiometric dynamic range and the reduced impact in errors in estimated aerosol optical depth range in this spectral channel.
- As expected, the match between AVHRR and TM data was much better at the surface than at TOA; this is

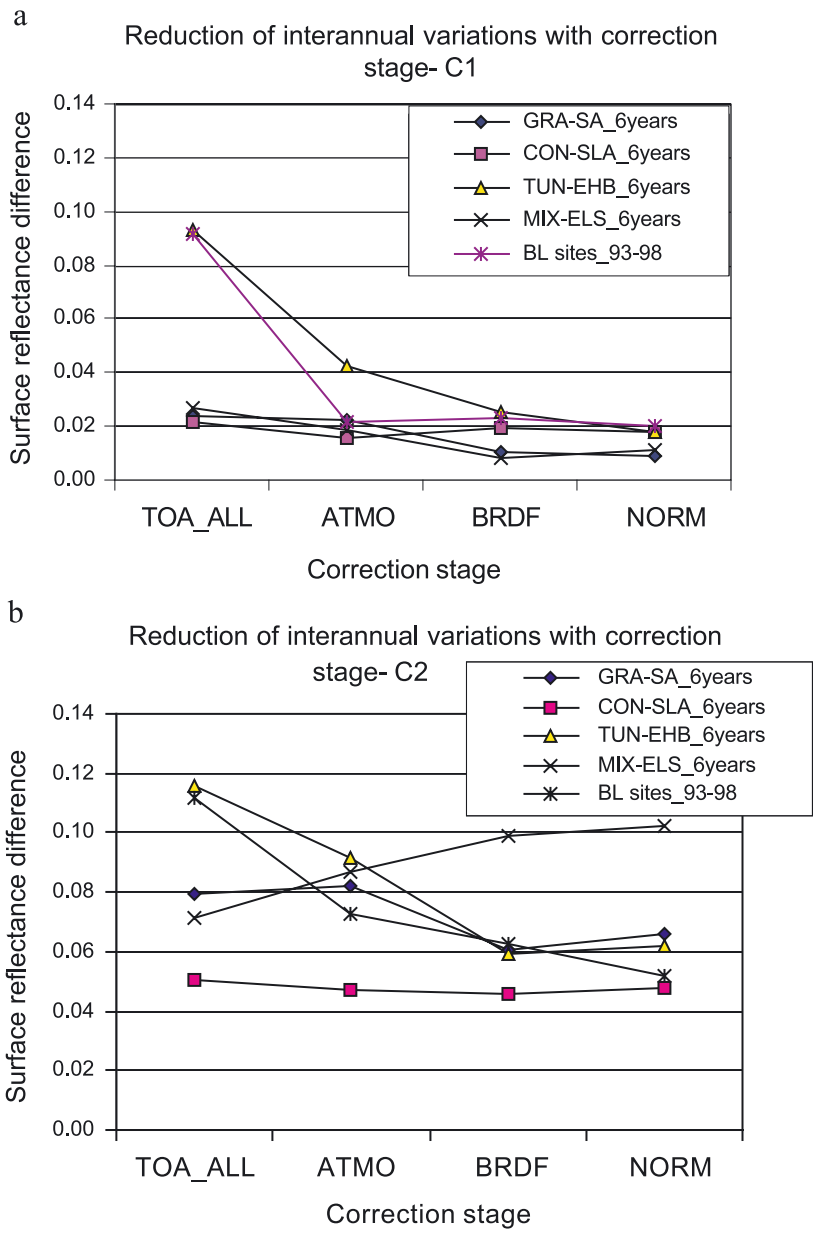

Fig. 4. The changes in the interannual range (1993–1998) at various correction stages. (a) Channel 1, (b) channel 2, (c) NDVI. Legend GRA-SA Grassland—Southern Alberta, CON-SLA Conifer—South of Lake Athabaska, TUN-EHB Tundra—East of Hudson Bay, MIX-ELS mixed wood forest—East of Lake Superior, BL sites Baren Land—sites Melville Island, Ungava Peninsula, District of Keewatin.

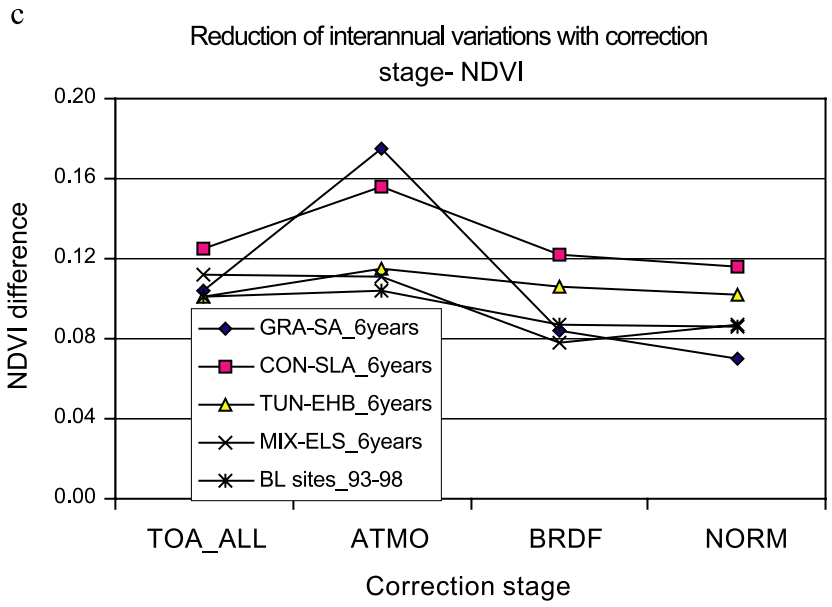

Fig. 4 (*continued*).

evident from both r^2 and regression slope values. Although the same TM-derived values were used in both cases, the better results at the surface nevertheless reflect the impact of the corrections.

- The effectiveness of the corrections is also evident from the coefficient of variability (CV, standard deviation from the regression line divided by the mean). Computing an average for the two scenes, CV remained about the same for C1 but decreased by ~40% for C2 and ~30% for NDVI (from 10% to 7%, Table 1). The values of 5% and 9% for NDVI are especially encouraging.
- ABC3V2 represents a significant improvement compared to the original ABC3 (refer to the last three lines in Table 1). Comparing an average for the two scenes with the results of a test for the first version (Cihlar, Ly, et al., 1997), the improvement is especially large in AVHRR C1 (170% in slope, 800% in r^2), but also significant (25–75%) for C2 and for NDVI (30–50%). The coefficient of variability also decreased, by 51–113% depending on the channel (Table 1). Note that the original comparison was made against single date AVHRR images resampled to 1 km, while here the reference data are from TM and the approximate AVHRR field of view. Therefore, the spatial extent is comparable in both cases but the radiometric quality of the TM-derived data should be superior. These results indicate that the improved correction procedures embedded in ABC3V2 have removed a much greater portion of the noise remaining in the original composites.

The reason for the AVHRR reflectances being higher than the corresponding TM values is not clear. Since the two data sets were obtained at nearly the same time and the corrections are made to a similar viewing geometry ($\theta_s = 45°$, $\theta = 0°$), BRDF corrections are not a likely cause. As noted above, it could be due to the incomplete atmospheric corrections at the higher view zenith angles. Other reasons could be residual subpixel contamination that was not detected by CECANT. Note, however, that the slope deviated substantially more at the TOA level (Table 1) compared to the surface; thus, the corrections have the intended impact but are not able to match the TM data completely.

4.2. Assessment of interannual consistency

Another measure of the quality of the corrections is an evaluation of the ability to detect interannual differences. Cihlar et al. (1998) performed a study of the interannual differences in ABC3 data. They found that over a four-year period and assuming that reflectance should remain constant for 'bare land' areas, the residual uncertainty was ±0.012, ±0.024, and ±0.038 for C1, C2, and NDVI, respectively. We repeated the comparison with the ABC3V2 data for the same geographic areas. Briefly, the procedure was as follows. Several sites with various dominant land cover types were selected based on a land cover map of Canada derived from 1995 AVHRR data (Cihlar et al., 1999), although these sites contain other land cover types as well. In each area the means per channel were computed for the period June 1 to August 31 of each year. The calculation was made using data at four processing stages: TOA which included only sensor calibration and conversion from radiance to reflectance; after atmospheric corrections, thus representing the surface reflectance (ATMO); after BRDF corrections which accounted for differences in imaging geometry (BRDF); and after interpolation where the contaminated pixels were replaced by temporal interpolation (NORM). For TOA and NORM,

means were computed for all land pixels, but in case of ATMO and BRDF, only uncontaminated land pixels were included in computing the mean value. In contrast to the earlier paper, we used all 1 km^2 pixels within the test areas.

Fig. 4 compares the difference between the maximum and the minimum values per site. It was derived by computing the mean value for each year over the July to August time period, and then determining the range between the highest and the lowest mean values.

Fig. 4a shows the effect of the various correction steps on channel 1. The interannual range decreased greatly ($0.09 \rightarrow 0.02$) for land cover types with minimum vegetation (barren, tundra), substantially for seasonally variable vegetation (mixed forest, grassland; $\sim 0.03 \rightarrow \sim 0.01$), and little for coniferous forest. It should be noted that the first correction step combines the effects of atmospheric corrections and the exclusion of contaminated pixels from the computation, thus explaining the much larger decrease for the non-vegetated land cover types, which occur mostly in the North. For barren land (the curve represents an average of four sites), the corrections reduced the range between highest and lowest mean value by 80% over the 6-year period. The other sites varied more (by up to 0.02 after corrections), but again the range was reduced by 67% for mixed forest and 63% for grassland. The decrease in the interannual range for the coniferous forest site was $\sim$ 15%.

In general, the results for C2 were similar in trend to C1 but smaller in magnitude. The main difference was that interannual differences decreased for C2 (Fig. 4b), between 5% and 46% for vegetated land cover types other than mixed forest where it increased by 44%. The reduction for bare land was also smaller, 43%. The difference between C1 and C2 is probably due to the generally higher C2 reflectance for the land cover types considered, and thus the effect of the initial pixel contamination is smaller. The increase in the mixed forest occurred as a combination of atmospheric and BRDF corrections (Fig. 4b).

Fig. 4c shows the behaviour of NDVI. As expected, the atmospheric corrections alone increased the interannual variations, which were subsequently reduced through BRDF corrections. Overall, the interannual range was similar among the different land cover types and not much reduced after the corrections compared to TOA; however, the reduction was still considerable given the increased range after atmospheric corrections.

While changes might be expected in vegetated areas due to interannual variations, they should be small for barren land. Even though this land cover type may contain small amounts of vegetation (Cihlar et al., 1999), they should not cause large changes in spectral reflectance, especially when averaged over all the test areas. The interannual variation of ~ 0.08 thus suggests that the data corrections did not remove at least a part of the noise. The residual barren land noise for the 6-year period (0.086) is similar to that for a 4-year period (0.068) in the original ABC3 version (Cihlar et al., 1998).

The above results indicate that overall, the modified procedure generally improved the interannual consistency of the data. However, the increase was not consistent among land cover types. Fig. 5 shows the change of the interannual range (4 years) between the two correction procedures. While the C1 radiometric dynamic range decreased for all sites (negative change), it increased substantially for C2 at vegetated sites. These changes led to an increase in the NDVI dynamic range for barren land and to a small overall change among all the sites. The reasons for an increased C2 range are not clear, but it is likely that it reflects actual interannual differences in the vegetation dynamics. This is supported by the good fit of the BRDF models (among vegetated types, average $r^2 = 0.75$ for C1, $r^2 = 0.78$ for C2; Latifovic et al., in press) compared to the BRDF models in the original ABC3 version as well as the more sensitive detection of contaminated pixels (Cihlar, Du, et al., in press).

A further examination of the data indicates that the interannual range after corrections increased with the length of the time series. For example, Fig. 6 shows the average range of NDVI values for segments of various lengths k. The range was computed the same way as in Fig. 4, except that various combinations of k years were drawn from the 6-year period to establish the average interannual range. In addition to the July to August time period, the computations were also made for the whole growing season (April 11 to October 31). Fig. 6 indicates a linear increase for the various combinations, although it should be noted that the number of available samples decreases for the larger k. The data also suggest that both vegetated and non-vegetated land cover types behaved in a similar way. However, this is inconsistent with the expected temporal stability of barren land reflectance since in this case, the range should be nearly constant. The offset for barren land between summer-only and whole

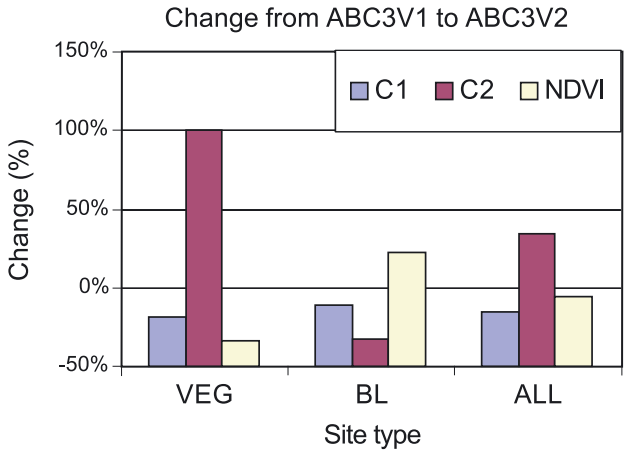

Fig. 5. Change in the interannual range (1993–1996) between ABC3 versions 1 and 2 for vegetated cover (forest, tundra) and barren land.

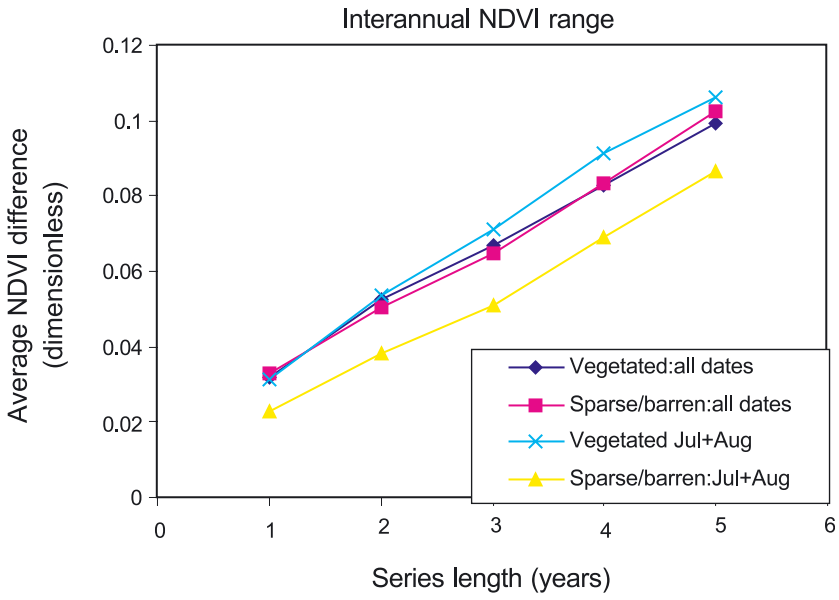

Fig. 6. The interannual variability of mean NDVI values for vegetated and barren land cover types for 1993–1998.

season implies that at least a part of the explanation for the interannual differences is in incomplete corrections. Most of the barren or sparsely vegetated areas are at high latitudes where all the corrections (atmospheric corrections, BRDF corrections, and the detection of contaminated pixels and replacement by interpolation) are difficult given the extreme viewing geometry, short snow-free season, and the paucity of quality ancillary data needed for the corrections. In addition, few clear sky/snow-free observations are available (and then mostly in the peak for the growing season), and thus the reconstitution of surface reflectance may be subject to considerable uncertainty (Cihlar, Beaubien, et al., 1997; Cihlar, Chen, et al., 1997; Cihlar, Ly, et al., 1997). Land cover of the BOREAS Region from AVHRR and Landsat data.

Although the offset in Fig. 6 (attributable to the greater interannual dynamics of vegetation) is relatively small (~ 0.02), two other factors also need to be taken into account. First, NDVI is very sensitive to a potential green vegetation increase in sparsely vegetated types, and this could increase the interannual range. Second, the trends are less reliable for the longer periods because of the limited sample size. These factors suggest that using barren land as a measure of the improvement may not be appropriate, and other options need to be considered.

5. Summary and conclusions

For quantitative studies of vegetation dynamics, satellite data need to be corrected for spurious effects that confound the signal of interest. In this study, we have applied several changes to an earlier AVHRR processing methodology to better represent the various physical processes that cause contamination of the AVHRR measurements. The modified procedure ABC3V2 improved the accuracy of AVHRR reflectance estimates, both in the sensitivity (slope) of the regression and in r^2. Compared to the TM-derived reference values, the corrected AVHRR estimates have average standard errors values of ± 0.009 for AVHRR C1, ± 0.019 for C2, and ± 0.04 for NDVI; the corresponding r^2 values were 0.55, 0.8, and 0.5, respectively. It should be noted that these comparisons relate to the AVHRR field of view. ABC3V2 reduced the interannual variation for barren land cover and increased it for vegetated land cover types. The impact of introducing the various improvements was considerable, especially for C1 where it greatly improved both r^2 and the estimated absolute values.

Although the changes in ABC3V2 significantly improved the estimated AVHRR surface reflectance, they nevertheless were not able to remove interannual variability for northern land cover types. It would be expected that these land cover types with little or no vegetation remain stable over time. This appears to be due to several factors including the short snow-free season, significant atmospheric contamination in the composites, and the extreme sun-surface-sensor geometry introducing uncertainties in the modelled atmospheric corrections. Additional factors, including errors in the estimated atmospheric parameters at the time of imaging, are likely contributing factors but this could not be confirmed with the available data. It is also possible that the knowledge of the sensor calibration is not sufficient to fully account for interannual variations. Further examination of these factors and their implications on long-term interannual studies of boreal vegetation dynamics is required.

The remaining interannual differences in C1, C2, and NDVI in the 1993–1998 ABC3V2-corrected data warrant

further attention, particularly for the barren land cover types. Any of the three critical processing steps (calibration, atmospheric correction, and BRDF correction) or their combination could be responsible. In addition, the variable field of view of the AVHRR pixel, the compositing process, and incomplete contaminated pixel screening may contribute to uncertainty in the data products. The interannual differences are a subject of a continuing study.

References

Barbosa, P. M., Gregoire, J. -M., & Pereira, J. M. C. (1999). An algorithm for extracting burned areas from time series of AVHRR GAC data applied at a continental scale. *Remote Sensing of Environment*, *69*, 253–263.

Barnes, W. L., Pagano, T. S., & Salomonson, V. V. (1998). Prelaunch characteristics of the moderate resolution imaging spectroradiometer (MODIS) on EOS-AM1. *IEEE Transactions on Geoscience and Remote Sensing*, *36*, 1088–1100.

Chen, J., Chen, W., Liu, J., Cihlar, J., & Gray, S. (2000). Annual carbon balance of Canada's forests during 1895–1996. *Global Biogeochemical Cycles*, *14*, 839–850.

Chen, J. M., & Cihlar, J. (1997). A hotspot function in a simple bidirectional reflectance model for satellite applications. *Journal of Geophysical Research*, *102*(D22), 25907–25913.

Chen, J. M., & Leblanc, S. G. (1997). A four-scale bidirectional reflectance model based on canopy architecture. *IEEE Transactions on Geoscience and Remote Sensing*, *35*, 1316–1337.

Chen, J. M., Pavlic, G., Brown, L., Cihlar, J., Leblanc, S. G., White, P., Hall, R. J., Peddle, D., King, D. J., Trofymow, J. A., Swift, E., Van der Sanden, J., & Pellikka, P. (2000). Validation of Canada-wide leaf area index maps using ground measurements and high and moderate resolution satellite imagery. *International Journal of Remote Sensing* (in press).

Chen, W. J., Chen, J. M., Price, D. T., Cihlar, J., & Liu, J. (2000). Carbon offset potentials of four alternative forest management strategies in Canada: A simulation study. *Mitigation and Adaptation Strategies for Global Change*, *5*, 143–169.

Cihlar, J. (1996). Identification of contaminated pixels in AVHRR composite images for studies of land biosphere. *Remote Sensing of Environment*, *56*, 149–163.

Cihlar, J., Beaubien, J., Latifovic, R., & Simard, G. (1999). Land Cover of Canada 1995 Version 1.1. Digital data set documentation. Ottawa, Ontario: Natural Resources Canada.

Cihlar, J., Beaubien, J., Xiao, Q., Chen, J., & Li, Z. (1997). Land cover of the BOREAS Region from AVHRR and Landsat data. *Canadian Journal for Remote Sensing*, *23*(2), 163–175.

Cihlar, J., Chen, J., & Li, Z. (1997). Seasonal AVHRR multichannel data sets and products for studies of surface-atmosphere interactions. *Journal of Geophysical Research-Atmospheres*, *102*(D24), 29625–29640.

Cihlar, J., Chen, J., Li, Z., Huang, F., Latifovic, R., & Dixon, R. (1998). Can interannual land surface signal be discerned in composite AVHRR data? *Journal of Geophysical Research-Atmospheres*, *103*(D18), 23163–23172.

Cihlar, J., Du, Y., & Latifovic, R. (2000). Land cover dependence in the detection of contaminated pixels in satellite optical data. *IEEE Transactions on Geoscience and Remote Sensing* (in press).

Cihlar, J., Ly, H., Li, Z., Chen, J., Pokrant, H., & Huang, F. (1997). Multitemporal, multichannel AVHRR data sets for land biosphere studies: Artifacts and corrections. *Remote Sensing of Environment*, *60*, 35–57.

Cihlar, J., Tcherednichenko, I., Latifovic, R., Li, Z., & Chen, J. (2001). Impact of variable atmospheric water vapour content on AVHRR data corrections over land. *IEEE Transactions for Geoscience and Remote Sensing*, *39*(1), 173–180.

Eidenshink, J. C., & Faundeen, J. L. (1994). The 1 km AVHRR global land data set: First stages in implementation. *International Journal of Remote Sensing*, *15*(17), 3443–3462.

El Saleous, N. Z., Vermote, E. F., Justice, C. O., Townshend, J. R. G., Tucker, C. J., & Goward, S. N. (2000). Improvements in the global biospheric record from the advanced very high resolution radiometer (AVHRR). *International Journal of Remote Sensing*, *21*, 1251–1277.

Fallah-Adl, H., Jaja, J., & Liang, S. (1997). Fast algorithms for estimating aerosol optical depth and correcting thematic mapper (TM) imagery. *Journal of Supercomputing*, *10*, 315–330.

Fedosejevs, G., O'Neill, N. T., Royer, A., Teillet, P. M., Bokoye, A. I., & McArthur, B. (2000). Aerosol optical depth for atmospheric correction of AVHRR composite data. *Canadian Journal for Remote Sensing*, *26*, 273–284.

Fraser, R. H., Li, Z., & Cihlar, J. (2000). Hotspot and NDVI differencing synergy (HANDS): A new technique for burned area mapping over boreal forest. *Remote Sensing of Environment*, *74*, 362–375.

Gesell, G. (1989). An algorithm for snow and ice detection using AVHRR data: An extension to the APOLLO software package. *International Journal of Remote Sensing*, *10*, 897–905.

Guindon, B. (1985). Automated control point acquisition in radar-optical image registration. *Canadian Journal for Remote Sensing*, *11*(1), 103–112.

Gutman, G. (1994). Normalisation of multi-annual global AVHRR reflectance data over land surfaces to common sun-target geometry. *Advances in Space Research*, *14*, 121–124.

Hay, J. E. (1985). Estimating solar irradiance on inclined surfaces: A review and assessment of methodologies. *International Journal for Solar Energy*, *3*, 203–240.

Herman, J. R., Bhartia, P. K., Wellemeyer, C. G., Seftor, C. J., Jaross, G., Schlesinger, B. M., Torres, O., Labow, G., Byerly, W., Taylor, S. L., Swissler, T., Cebula, R. P., & Gu, X. -Y. (1996). *Meteor-3 total ozone mapping spectrometer (TOMS) data products user's guide*, NASA Ref. Pub., 53pp. [Available from NASA Goddard Space Flight Centre, Greenbelt, MD 20771].

Holben, B. N. (1986). Characteristics of maximum-value composite images from temporal AVHRR data. *International Journal for Remote Sensing*, *7*, 1417–1434.

Holben, B. N., & Shimabukuro, Y. E. (1993). Linear mixing model applied to coarse spatial resolution data from multi-spectral satellite sensors. *International Journal of Remote Sensing*, *14*, 2231–2240.

Iqball, M. (1983). *An introduction to solar radiation*. New York: Academic Press, 390 pp.

Kalnay, E., Kanamitsu, M., Kisler, R., Collins, W., Deaven, D., Gandin, L., Iredell, M., Sasha, S., White, G., Woolen, J., Zhu, Y., Chelliah, M., Ebisuzaki, W., Higgins, W., Janowiak, J., Mo, K. C., Ropelewski, C., Wang, J., Leetmaa, A., Reynolds, R., Jenne, R., & Joseph, D. (1996). The NCEP/NCAR 40-year reanalysis project. *Bulletin of the American Meteorological Society*, *77*, 437–471.

Kaufman, Y. J., & Remer, L. A. (1994). Detection of forests using mid-IR reflectance: An application for aerosol studies. *IEEE Transactions on Geoscience and Remote Sensing*, *32*, 672–683.

Kidwell, K. B. (Ed.) (1998). *NOAA polar orbiter data user's guide.* Washington, DC: NOAA-NESDIS, http://www2.ncdc.noaa.gov/docs/podug/.

Kondratyev, K. Ya. (1977). *Radiation regime of inclined surfaces.* Technical Note No. 152, WMO-467, Geneva, 82 pp.

Latifovic, R., Cihlar, J., & Chen, J. (2003). A comparison of BRDF models for the normalisation of satellite optical data to a standard sun-target-sensor geometry. *IEEE Transcription on Geoscience and Remote Sensing*, *41*(8), 1889–1898.

Liu, J., Chen, J. M., Cihlar, J., & Chen, W. (1999). Net primary productivity distribution in the BOREAS study region from a process model driven by satellite and surface data. *Journal of Geophysical Research*, *104*(D22), 27735–27754.

Liu, J., Chen, J. M., Cihlar, J., & Park, W. (1997). A process-based boreal

ecosystem productivity simulator using remote sensing inputs. *Remote Sensing of Environment*, *62*, 158–175.

Los, S. O., Justice, C. O., & Tucker, C. J. (1994). A global 1° by 1° NDVI data set for climate studies derived from the GIMMS continental NDVI data. *International Journal of Remote Sensing*, *15*, 3493–3518.

McPeters, R. D., Bhartia, P. K., Krueger, A. J., Herman, R. J., Wellemeyer, C. G., Seftor, C. J., Jaross, G., Torres, O., Moy, L., Labow, G., Byerly, W., Taylor, S. L., Swissler, T., & Cebula, R. P. (1998). Earth probe total ozone mapping spectrometer (TOMS) data product user's guide. *NASA Technical*, 1998–206895.

Pereira, J. M. C. (1999). A comparative evaluation of NOAA/AVHRR vegetation indexes for burned surface detection and mapping. *IEEE Transactions on Geoscience and Remote Sensing*, *37*, 217–226.

Proy, C., Tanre, D., & Deschamps, P. Y. (1989). Evaluation of topographic effects in remotely sensed data. *Remote Sensing of Environment*, *30*, 21–32.

Rahman, H., & Dedieu, G. (1994). SMAC: A simplified method for the atmospheric correction of satellite measurements in the solar spectrum. *International Journal of Remote Sensing*, *15*, 123–143.

Richter, R. (1998). Correction of satellite imagery over mountainous terrain. *Applied Optics*, *37*, 4004–4015.

Robertson, B., Erickson, A., Friedel, J., Guindon, B., Fisher, T., Brown, R., Teillet, P., D'Iorio, M., Cihlar, J., & Sancz, A. (1992). GEOCOMP, a NOAA AVHRR geocoding and compositing system. *Proceedings of the ISPRS Conference, Commission 2, Washington, DC* (pp. 223–228).

Roger, J. C., & Vermote, E. F. (1998). A method to retrieve the reflectivity signature at 3.75 μm from AVHRR data. *Remote Sensing of Environment*, *64*, 103–114.

Roujean, J. -L., Leroy, M., & Deschamps, P. -Y. (1992). A bidirectional reflectance model of the earth's surface for the correction of remote sensing data. *Journal of Geophysical Research*, *97* (D18), 20455–20468.

Roy, D. P., Giglio, L., Kendal, J. K., & Justice, C. O. (1999). Multitemporal active-fire based burn scar detection algorithm. *International Journal of Remote Sensing*, *20*, 1031–1038.

Ruff, I., & Gruber, A. (1983). Multispectral identification of clouds and earth surfaces using AVHRR data. *Proceedings of the 5th Conference on Atmospheric Radiation, Baltimore, MD, October 31–November 4* (pp. 475–478). Boston, MA: American Meteorological Society.

Saint, G. (1992). *VEGETATION onboard SPOT 4, Mission specifications.* Report LERTS No. 92102, Laboratoire d'etudes et de recherches en teledetection spatiale, Toulouse, France, 40 pp.

Sandmeier, S., & Itten, K. I. (1997). A physically-based model to correct atmospheric and illumination effects in optical satellite data of rugged terrain. *IEEE Transactions on Geoscience and Remote Sensing*, *35*, 708–717.

Sellers, P. J., Los, S. O., Tucker, C. J., Justice, C. O., Dazlich, D. A., Collatz, J. A., & Randall, D. A. (1994). A global 1° by 1° NDVI data set for climate studies: Part 2. The generation of global fields of terrestrial biophysical parameters from the NDVI. *International Journal of Remote Sensing*, *15*, 3519–3545.

Spencer, J. W. (1971). Fourier series representation of the position of the Sun. *Search*, *2*, 172.

Teillet, P., Guindon, B., & Goodenough, D. G. (1982). On the slope-aspect correction of multispectral scanner data. *Canadian Journal for Remote Sensing*, *8*, 84–106.

Townshend, J. R. G. (1994). Global data sets for land applications for the advanced very high resolution radiometer: An introduction. *International Journal of Remote Sensing*, *15*(17), 3319–3332.

Townshend, J. R. G., Huang, C., Kalluri, S. N. V., DeFries, R. S., & Liang, S. (2000). Beware of per-pixel characterisation of land cover. *International Journal of Remote Sensing*, *21*, 839–843.

Vermote, E. F., Tanre, D., Deuze, J. L., Herman, M., & Mocrette, J. -J. (1997). Second simulation of the satellite signal in the solar spectrum: 6S: An overview. *IEEE Transactions on Geoscience and Remote Sensing*, *34*, 675–686.

Wu, A., Li, Z., & Cihlar, J. (1995). Effects of land cover type and greenness on AVHRR bidirectional reflectances: Analysis and removal. *Journal of Geophysical Research*, *100*, 9179–9192.